Thermal equation of state of Fe3O4 magnetite up to 16 GPa and 1100 K

Nicki C. Siersch, Giacomo Criniti, Alexander Kurnosov, Konstantin Glazyrin, Daniele Antonangeli

Thermal equation of state of Fe_3O_4 magnetite up to 16 GPa and 1100 K

Nicki C. Siersch[1,*], Giacomo Criniti[2], Alexander Kurnosov[2], Konstantin Glazyrin[3], Daniele Antonangeli[1]

[1] Sorbonne Université, Muséum National d'Histoire Naturelle, UMR CNRS 7590, Institut de Minéralogie, de Physique des Matériaux et de Cosmochimie, IMPMC, Paris, France.

[2] Bayerisches Geoinstitut, Universität Bayreuth, D-95440 Bayreuth, Germany.

[3] Deutsches Elektronen-Synchrotron DESY, Notkestr. 85, D-22607 Hamburg, Germany.

[*] Corresponding author: nsiersch@gmail.com

Abstract

Fe_3O_4 magnetite is an important mineral commonly found in various geological settings, including the planet Mars, whose thermo-elastic properties at high pressure and temperature are still poorly constrained. We performed X-ray diffraction measurements on natural magnetite using resistive-heated diamond anvil cells up to 16 GPa and 1100 K. We fitted a thermal equation of state (EoS) to the collected data resulting in K_0 = 182(1) GPa, K'_0 = 4, θ_D = 660 K, γ = 1.8(1), and q = 2.7. Moreover, it was possible to explore the structural evolution of magnetite in detail using single-crystal measurements. Over the studied pressure and temperature range, we found no evidence of a transformation from an inverse to a normal spinel structure. The EoS parameters obtained in this study will allow to be implemented into currently available databases for self-consistent thermodynamic modeling. In particular, the obtained results are used to model and compare the sound wave velocities of a magnetite-bearing and magnetite-free Martian upper mantle assemblage. We observe that the incorporation of

magnetite reduces the sound wave velocities, however, the magnitude of the effect is below the current seismic detection limit of the InSight mission on Mars at the low abundance of magnetite expected in the Martian mantle.

Keywords: magnetite, thermal equation of state, X-ray diffraction, high-pressure, high-temperature

Introduction

Magnetite (α-Fe_3O_4) is an important mineral commonly found in igneous, sedimentary and metamorphic rocks of the Earth and in meteorites, which also finds industrial applications, going from being a traditional recording medium to the emerging field of spin electronics. Magnetite was also recently suggested to be potentially stable in the most oxidized regions of the upper mantle of Mars (Xu et al. 2021). Magnetite crystallizes at ambient pressure in a cubic structure above the Verwey temperature of $T_V \sim 120$ K (Verwey 1939), in the space group $Fd\bar{3}m$ with Z = 8. It has an inverse spinel structure with the tetrahedrally-coordinated sites being fully occupied by Fe^{3+}, whereas the remaining Fe^{2+} and Fe^{3+} are randomly distributed between the octahedrally-coordinated sites ($[Fe^{3+}]_T[Fe^{2+}Fe^{3+}]_OO_4$). This is in contrast to a normal spinel structure where the tetrahedrally-coordinated sites are occupied by the divalent cation and the octahedrally-coordinated sites are filled with the trivalent cation. With increasing pressure, magnetite was found to undergo a gradual phase transformation to the so-called h-Fe_3O_4 (Mao et al. 1974; Huang and Bassett 1986; Fei et al. 1999; Haavik et al. 2000; Lazor et al. 2004) or, following a newer nomenclature, β-Fe_3O_4 (Khandarkhaeva et al. 2022). Mao et al. (1974) were the first to report the transformation from magnetite to β-Fe_3O_4 above 25 GPa as observed by powder X-ray diffraction in a diamond anvil cell (DAC). The transformation was described to

be sluggish, especially at ambient temperature, with the completion of the phase transformation being faster at 600 K. These findings were confirmed by the study of Huang and Bassett (1986), which reported a large two-phase hysteresis upon compression and decompression. The structure of β-Fe_3O_4 was initially suggested to be monoclinic (Mao et al. 1974), but subsequent Rietveld refinements performed on powdered magnetite in a resistively-heated DAC proposed β-Fe_3O_4 to have the orthorhombic $CaMn_2O_4$-type structure in the space group *Pbcm* (Fei et al. 1999). A more recent study by Haavik et al. (2000) confirmed β-Fe_3O_4 to be orthorhombic, but having the $CaTi_2O_4$-type structure in the space group *Cmcm*. This structure was further confirmed by Lazor et al. (2004) who also performed Rietveld refinements on polycrystalline magnetite and a recent study by Khandarkhaeva et al. (2022), who performed single-crystal X-ray diffraction experiments in laser-heated DACs. The latter also reported two new Fe_3O_4 polymorphs, namely γ-Fe_3O_4 having the Yb_3S_4-type structure in space group *Pnma* stable at 64-73 GPa upon heating at 1500-2000 K, and δ-Fe_3O_4 having the Th_3P_4-type structure in space group $I\bar{4}2d$ stable at 78(1) GPa and 4800(300) K (Khandarkhaeva et al. 2022).

In the stability field of α-Fe_3O_4 at pressures below the structural transformation into β-Fe_3O_4, the material retains the cubic structure. However, within this pressure range, the electronic state of magnetite is quite controversial. Several studies using Mössbauer spectroscopy and powder X-ray diffraction introduced the notion of a possible coordination crossover in the magnetite structure, with the electronic charge density shifting from the octahedral to tetrahedral sites, hence inducing an inverse to normal spinel transition (Pasternak et al. 2003; Rozenberg et al. 2007). Above 7 GPa, magnetite is suggested to first transform from an inverse spinel to an intermediate state, and then to a normal spinel above 17 GPa at 300 K (Pasternak et al. 2003; Rozenberg et al. 2007). The same process was observed with decreasing temperature (Pasternak et al. 2003). A more recent investigation by single-crystal XRD and Mössbauer spectroscopy (Glazyrin et al. 2012), however, could not confirm these observations and the proposed

scenario, at least up to a pressure of 25 GPa at 300 K. An additional magnetic transition was proposed by Ding et al. (2008) who, based on Fe K-edge X-ray magnetic circular dichroism measurements, suggested a high-spin to intermediate-spin transition of the Fe^{2+} ions between 12 and 16 GPa that, noteworthy, is incompatible with an inverse to normal spinel transition as described by Pasternak et al. (2003) and Rozenberg et al. (2007). Glazyrin et al. (2012) found the volume change associated to such a transition too small to be resolved with single-crystal XRD, and further found no evidence for a spin transition in their Mössbauer spectroscopy data. Additional investigations are needed to confirm the existence and clarify the nature of these pressure- and/or temperature-induced modifications affecting either electronic or magnetic degrees of freedom, also as a function of different pressure media and the effects of non-hydrostatic conditions.

Recently, experimental studies confirmed the presence of magnetite next to majoritic garnet in Earth's mantle assemblages (Tao et al. 2018) and in equilibrium with pyroxene and olivine in upper mantle assemblages representative for Mars (Xu et al. 2021) making it even more relevant to investigate the thermo-elastic properties of magnetite. Until now, the elastic properties of magnetite have been determined only at room temperature using a large number of different techniques including powder X-ray diffraction (e.g. Mao et al. 1974; Haavik et al. 2000 and references therein; Lazor et al. 2004; Rozenberg et al. 2007), single-crystal X-ray diffraction (e.g. Finger et al. 1986; Nakagiri et al. 1986; Kuriki et al. 2002; Reichmann and Jacobsen 2004; Gatta et al. 2007; Glazyrin et al. 2012) and ultrasonic interferometry (e.g. Reichmann and Jacobsen 2004). The bulk modulus K_0 obtained in the above-mentioned studies fall in a large range between 141 and 222 GPa, with its pressure derivative K'_0 ranging between 3.6 and 7.5. Once limiting to studies performed after the year 2000, predominantly conducted using single-crystal XRD (Reichmann and Jacobsen 2004; Gatta et al. 2007; Glazyrin et al. 2012) and powder XRD (Rozenberg et al. 2007), results are more comparable, with K_0 between 180 and

189 GPa and K'_0 in the range 3.6 to 5.2. Until now, only one study (Lazor et al. 2004) attempted to determine the compressibility of magnetite at high temperatures, without reporting the actual data. The thermo-elastic properties of magnetite, however, are critically needed, for example to be able to model density and wave velocities through a magnetite-bearing phase assemblage, e.g. representing the Martian upper mantle (Xu et al. 2021).

The aim of this study is two-fold: 1) to determine the thermal equation of state of Fe_3O_4 magnetite up to 16 GPa and 1100 K using X-ray diffraction combined with resistive-heated diamond anvil cells and 2) to investigate the structural evolution of magnetite in order to elucidate any structural changes leading towards a phase transformation at high pressure and temperature.

Methods

A natural magnetite sample grown on a mica schist bedrock sourced from Chester, Vermont, USA has been used as starting material for all powder and single-crystal measurements at high pressure and high temperature. The electron microprobe, operated at 15 keV and 10 nA with a focused beam, was calibrated using diopside as standard for Mg, Si and Ca, albite for Na, orthoclase for Al, Fe_2O_3 for Fe, Cr_2O_3 for Cr, and used to obtain the chemical composition of the natural magnetite. Analyses on 60 individual spots on a one-sided polished magnetite sample embedded in epoxy resulted in the chemical composition reported in Table 1, confirming the high purity of this natural magnetite sample. This natural sample is purer (99.5%) in comparison to the natural magnetite sample investigated by Glazyrin et al. (2012) having a purity of 99.2%. The sample was crushed dry in an agate mortar for 30 min until a fine-grained homogeneous powder was obtained.

High pressure and high temperature experiments were prepared and performed at the Extreme Conditions Beamline P02.2 of PETRA III (Hamburg, Germany) (Liermann et al. 2015). Two Mao-type symmetric DACs were prepared and dedicated to XRD measurements at high-pressure and ambient temperature on a single-crystal (run hereafter referred to as DAC_300Ksc) and on a powdered sample (DAC_300Kpwd), respectively. DAC_300Ksc was equipped with two Boehler-Almax diamonds (Boehler and De Hantsetters 2004) having a culet diameter of 400 µm. A 200 µm thick Re gasket was indented to 73 µm and a hole of 200 µm diameter was laser-drilled in the center of the indentation acting as sample chamber. A single-crystal of around 40x60x20 μm^3 was placed in the center of the culet next to a small ruby sphere acting as a fluorescence pressure gauge (Dewaele et al. 2004). DAC_300Kpwd was prepared with standard diamonds of 400 µm culet diameter. The Re gasket was prepared in the same way as described above. The powdered pelleted sample was placed inside the sample chamber together with a ruby sphere. Both DACs were gas-loaded with neon acting as quasi-hydrostatic pressure transmitting medium (Liermann et al. 2015) as it was reported to provide conditions as hydrostatic as helium gas up to at least 19 GPa at ambient temperature (Scheidl et al. 2016). During all experiments the pressure was increased remotely using a gas-driven membrane.

Three resistively-heated DACs (DAC_600K, DAC_900K and DAC_1100K) were prepared with one standard (upstream) and one Boehler-Almax diamond (downstream) each, employing diamonds of 300 µm culet for DAC_600K and DAC_900K and of 400 µm culet for DAC_1100K. A couple of 0.5 mm thick graphite heaters connected by two Mo electrodes built inside the DACs allowed generating stable high temperatures (designed after Lawrence Livermore 4-pin cells). Heaters from layered graphite surrounding the Re gasket are forming a homogenous heating field at the diamond tips and temperatures up to 1100 K inside the sample chamber. Re gaskets were pre-indented to a thickness of ~40-70 µm and sample chambers of 130-150 µm in diameter were drilled. The temperature was monitored using two individual R-

type thermocouples per DAC, positioned as close to the sample chamber as possible. The average of the two readings was assumed as the sample's temperature and the standard deviation was taken as uncertainty (Table 2). DAC_600K was loaded with a single-crystal magnetite sample and $SrB_4O_7:Sm^{2+}$ acting as pressure gauge throughout the experiment (Rashchenko et al. 2015). DAC_900K and DAC_1100K were loaded with a powdered and single-crystal magnetite sample, respectively, together with gold nano-powder for pressure determination (Dorogokupets and Dewaele 2007). For DAC_1100K fitting of 1D patterns was preferred at high pressure and temperature above 900 K because the quality of the single-crystal data was not ideal anymore. All three DACs were loaded with silicon oil as pressure transmitting medium, which provides a good compromise between hydrostaticity and risk of diamond failure events. Our experiment at 600 K confirmed the efficiency of silicon oil as quasi-hydrostatic pressure medium at high temperatures. The membrane-driven resistively-heated DACs were placed into a vacuum chamber, to avoid oxidation at high temperatures of graphite heaters, cell components and diamonds.

Reference values for the unit cell volumes of magnetite (both powder and single-crystal) and gold nano-powder, were measured at ambient conditions prior to the compression experiments, as well as the fluorescence lines of ruby and $SrB_4O_7:Sm^{2+}$. In this procedure, both the magnetite samples and the pressure standards were measured being placed inside the sample chamber of a DAC without any pressure transmitting medium. By employing an X-ray beam having a focused spot size of 8(H) x 3(V) μm^2 full width at half maximum (FWHM) at 25.6 keV, diffraction patterns of magnetite and gold nano-powder were recorded using a Perkin-Elmer XRD 1621 flat panel detector (Liermann et al. 2015). Polycrystalline CeO_2 and a single-crystal of natural enstatite ($Mg_{1.93}Fe_{0.06}Si_{1.93}Al_{0.06}O_6$, *Pbca*; a=18.2391(3) Å; b=8.8117(2) Å; c=5.18320(10) Å) were used to calibrate the sample to detector distance and the detector parameters for powder and single-crystal diffraction. Single-crystal diffraction data at high

pressure were collected upon continuous rotation of samples around a vertical axis (ω) between ±30° in steps of 0.5°. The acquisition time of each frame was 0.5 s/frame and a Pt absorber of 50 µm was used to avoid saturating the detector. Diffraction data used for precise lattice parameter determination from integrated 1D profiles were collected upon rotation of the DAC between ±20° in ω with an exposure time of 20 s and using a Pt absorber of 50 µm.

For the high-temperature runs, the samples were pre-compressed to a low starting pressure, within the silicon oil field of quasi-hydrostaticity. Then the temperature was increased to the target value and left to stabilize for half an hour. XRD patterns were collected upon compression every 1 to 2 GPa at a constant temperature up to ~14 GPa. For DAC_1100K, XRD patterns were collected every 100 K starting from 600 K while increasing to the target temperature of 1100 K. The collected diffraction data were integrated using DIOPTAS (Prescher and Prakapenka 2015) and analyzed using full profile LeBail refinements with the GSAS software package in the EXPGUI interface (Toby 2001; Larson and Von Dreele 2004). Processing of single-crystal diffraction data, which included orientation determination, indexing, intensity integration, correction for Lorentz and polarization factors, and empirical absorption correction based on spherical harmonics (ABSPACK), was carried out using *CrysAlisPro* 1.0.43 (Rigaku, Oxford Diffraction).

Structural refinements were performed for data collected in DAC_300Ksc, DAC_600K and for the first four points of DAC_1100K using the ShelXle software (Hübschle et al. 2011; Sheldrick 2015). Isotropic displacement parameters were used to reduce the number of refined parameters due to the limited number of reflections at high pressure and temperature in the DAC. Between 26 and 38 unique reflections could be used, depending on pressure and temperature to refine 5 individual parameters. Details of the structural refinements are reported in the deposited CIF and in Table S1.

Results and Discussion

P-V-T equation of state of Fe_3O_4 magnetite

The variation with pressure of the unit-cell volumes of magnetite at ambient temperature collected on a single-crystal and a powdered sample in two separate runs, normalized with respect to their room pressure values, shows a smooth decrease up 15.7 GPa, the highest pressure reached in this study (Figure 1a). Plotting the normalized stress F_E versus Eulerian finite strain f_E (Figure S1) shows a horizontal line over the entire pressure range. Therefore, a second-order Birch-Murnaghan equation of state (BM2 EoS) can be applied to fit the combined *P-V* data, normalized to the corresponding V_0, as implemented in the EoSfit7 GUI software (Angel et al. 2014; Gonzalez-Platas et al. 2016), resulting in an isothermal bulk modulus K_{T0} = 184(1) GPa with its pressure derivative K'_{T0} fixed to 4. Fit to a third-order BM EoS (BM3 EoS) gives comparable results, with K_{T0} = 181(3) GPa and K'_{T0} = 4.6(5). Fitting the two datasets individually with BM2 EoS results in values of K_{T0} of 183(1) GPa and 184(1) for powder and single-crystal data, respectively, thus, within mutual uncertainties. The unit-cell volumes reported by several studies (Finger et al. 1986; Nakagiri et al. 1986; Kuriki et al. 2002; Reichmann and Jacobsen 2004; Gatta et al. 2007; Rozenberg et al. 2007; Glazyrin et al. 2012) are in very good agreement with the *P-V* data collected in this study (Figure 1a). We note that all these studies, except for Rozenberg et al. (2007), were performed on synthetic or natural single-crystals and using quasi-hydrostatic pressure transmitting media such as a 4:1 methanol:ethanol mix for measurements below 4.5 GPa (Finger et al. 1986; Nakagiri et al. 1986), 16:3:1 methanol:ethanol:water below 9 GPa (Reichmann and Jacobsen 2004; Gatta et al. 2007) or neon up to 21 GPa (Glazyrin et al. 2012). The *P-V* data reported by Rozenberg et al. (2007) is the only study performed on powdered magnetite that is in agreement with our study, most likely because their data have been collected using helium as pressure transmitting medium, so under hydrostatic conditions. Four further studies by Mao et al. (1974), Haavik et

al. (2000), Kuriki et al. (2002) and Lazor et al. (2004) show a stiffer compression behavior, especially at pressures above ~10 GPa (Figure 1a). Three out of the four X-ray diffraction studies have been performed on powders in DACs, with the exception of Kuriki et al. (2002), who performed measurements on a single-crystal. Employed pressure-transmitting media, namely N_2 (Haavik et al. 2000), NaCl (Mao et al. 1974; Lazor et al. 2004) and a methanol:ethanol mixture (Kuriki et al. 2002) are known to have low hydrostatic limits of 3-10.5 GPa (N_2 and NaCl, e.g. Angel et al. 2007; Klotz et al. 2009) and <4 GPa (methanol:ethanol, e.g. Piermarini et al. 1973; Otto et al. 1998). The stiffer compressibility reported in these studies might therefore arise from non-hydrostatic stresses developed upon compression, in particular at the highest pressures of the data collection. The observed behavior could also be explained by the effect of deviatoric stress resulting in 'pressure overestimation' when, although the sample volume is measured correctly, the corresponding pressure is systematically biased, e.g. due to a different stress on a pressure sensor (Glazyrin et al. 2016).

The unit-cell volumes of magnetite collected in this study along four isotherms, at 300 K, 600(50) K, 869(57) K and 1068(72) K, are reported in Table 2 and illustrated in Figure 1b. The expected increase of the unit-cell volume with increasing temperature is well visible. The single-crystal and powder data (represented by open and closed circles, respectively) collected up to 1070 K (DAC_1100K) every 100 K starting from 600 K are in good agreement with the volumes collected in the runs DAC_600K and DAC_900K within uncertainties. The entire *P-V-T* dataset was fitted by a BM2 EoS combined with a Mie-Grüneisen-Debye (MGD) model for the thermal pressure, using the EoSfit7 GUI software (Angel et al. 2014; Gonzalez-Platas et al. 2016) to obtain V_0 and K_{T0} and the high-temperature parameters, namely the Debye temperature θ_D, the Grüneisen parameter γ and its logarithmic volume derivative q. We took advantage of the q-compromise Mie-Grüneisen-Debye approach implemented in EoSfit7 GUI (Angel et al. 2020) in order to reduce the number of fitting parameters and the otherwise large

correlation of q with γ in the relatively limited pressure and temperature range targeted in this study. Still, refining K_0, θ_D, and γ was yielding larger correlations and thus uncertainties, especially for θ_D and γ (θ_D = 1397(865) K with V_0 = 44.604(7) cm^3/mol, K_0 = 182(1) GPa and $\gamma = 2.3(8)$). The value of θ_D was therefore fixed to 660 K (Kouvel 1956) which is also in agreement with the Debye temperature calculated for an Fe oxide having a mean atomic mass of ~29 (Stixrude and Lithgow-Bertelloni 2011). The final fitting results are V_0 = 44.603(7) cm^3/mol, K_0 = 182(1) GPa and γ = 1.8(1) (solid lines in Figure 1b). In order to test the influence of q on γ, the fitting procedure was repeated with q fixed to 2.7, the value proposed by Stixrude and Lithgow-Bertelloni (2005, 2011) for the two spinels reported in their database, namely the spinels $MgAl_2O_4$ and $FeAl_2O_4$. The resulting fitting parameters were exactly the same as the results obtained from the q-compromise approach reported above.

Structural evolution of Fe_3O_4 magnetite at high pressure and high temperature

Single-crystal data collected along the two isotherms at 300 K and 600 K and four additional points obtained while increasing the temperature in the DAC to 1100 K have been used to refine the structure of magnetite at high pressure and temperature. Figure 2a shows the evolution of the polyhedral volumes, namely the octahedral and tetrahedral volumes, with increasing pressure at room temperature. Both data sets at 300 K were fit to a BM2 EOS resulting in bulk moduli $K_{0,tet}$ and $K_{0,oct}$ of 210(13) and 169(4) GPa, respectively. The compressibility of the tetrahedra is therefore smaller compared to compressibility of the octahedra. The here-measured compressibilities are in agreement with the values expected according to a model based on ionic potential (IP=valence state/ionic radius) proposed by Bruschini et al. (2015), namely $K_{0,tet}$ and $K_{0,oct}$ of 230 and 180 GPa, respectively. Our measurements thus support the validity of this relatively simple model for predicting the bulk moduli for spinel compositions. Figure 2a also compares the evolution of polyhedral volumes with pressure to literature data obtained from

single-crystal (Finger et al. 1986; Gatta et al. 2007; Glazyrin et al. 2012) or powder XRD (Haavik et al. 2000; Rozenberg et al. 2007). The data collected in this study are in good agreement with the data reported by Glazyrin et al. (2012). The compressibility data by Gatta et al. (2007) shows slightly softer tetrahedral and stiffer octahedral volumes, respectively. Single-crystal data by Finger et al. (1986) are in very good agreement with the tetrahedral volumes reported in this study, whereas a stronger decrease with pressure for the octahedral volumes were observed. The compressibility of the tetrahedral site measured by Haavik et al. (2000) is in good agreement until ~ 16 GPa, but then becomes stiffer. The octahedral volumes already start deviating to a stiffer behavior above ~10 GPa. This directly reflects the stiffer behavior of the unit-cell volume above 10 GPa (Figure 1a), likely due to non-hydrostatic stresses in their DAC experiment (Haavik et al. 2000). The pronounced decrease and increase for octahedral and tetrahedral volumes starting from ~7 GPa reported by Rozenberg et al. (2007), which was ascribed to the onset of an inverse to normal spinel transition, is not supported by the present data set. However, as the pronounced changes reported by Rozenberg et al. (2007) are exactly opposite for tetrahedral and octahedral volumes inside the magnetite structure, the mean compressibility of the unit-cell volume is not influenced, resulting in the good agreement with the unit-cell volumes reported in this study (Figure 1a).

Figure 2b shows the polyhedral volumes versus pressure along the two isotherms measured in this study. As expected, the polyhedral volumes are slightly larger at high temperatures (Figure 2b), while temperature-induced softening is not clearly visible. No abrupt change in polyhedral volumes can be observed that could be linked to a phase transformation or a distinct structural change in magnetite. Furthermore, we performed a test on our structural refinement data allowing the site occupancy factor of Fe in octahedral coordination to be refined. Results show no evidence of a transformation to maghemite $(Fe^{3+}_{0.67}\square_{0.33})Fe^{3+}_{2}O_4$ upon heating, arguing against the possible oxidation of our samples during the high-temperature experiments.

The evolution of the oxygen coordinate *u*, controlling the individual volumes of tetrahedra and octahedra, was used by Rozenberg et al. (2007) to support their hypothesis of the onset of inverse to normal spinel transition. In Figure 3, we report the oxygen coordinate *u* versus pressure at 300 K, and the high-temperature single-crystal data collected in this study. The data points show an almost constant trend, with only a slight increase with pressure. We also note that, within uncertainties, the values of *u* are very similar for ambient temperature as well as for the high temperature datasets. This provides evidence that no normal spinel component appears upon heating in our samples. Our data are in good agreement with values reported in literature, which however generally have a larger scatter and larger uncertainties (Finger et al. 1986; Haavik et al. 2000; Glazyrin et al. 2012). The oxygen coordinates reported by Nakagiri et al. (1986) and Gatta et al. (2007) are smaller than the values obtained in this study and show a little decrease with pressure. Rozenberg et al. (2007) report oxygen coordinates that first decrease slightly up to pressures of ~5 GPa, then show a strong increase with a maximum around ~15 GPa, followed by a decrease up to 20 GPa. This behavior follows the same pressure evolution previously discussed for the tetrahedral volumes, and is not confirmed by the single-crystal data collected in this study nor by any other study on magnetite available in literature (Finger et al. 1986; Nakagiri et al. 1986; Haavik et al. 2000; Gatta et al. 2007; Glazyrin et al. 2012). Since the change in polyhedral volumes depend on a single coordinate of the O atoms inside the crystal structure of magnetite, data collected on a powder sample are often more difficult to analyze and more prone to misinterpretation. Rozenberg et al. (2007) could have experienced problems due to data quality, resulting in biased values produced by Rietveld refinements on their powdered magnetite sample. In particular, Glazyrin et al. (2012) suggested that the peculiar trend reported from a powder sample analysis by Rozenberg et al. (2007) could have originated from an insufficient number of diffracting crystallites potentially a with strong grain size hysteresis as well as from texture evolution. Our single-crystal results are consistent with

the single-crystal structural refinements shown in Glazyrin et al. (2012), and we consider that they resolve an important controversy.

Implications

Magnetite is commonly found as a stable phase in many geological contexts, however, until now, its thermal equation of state (*P*-*V*-*T* relations) was not experimentally determined. The mixed iron valence at the octahedral site makes magnetite also a challenge for calculations. As such the here-obtained thermal EoS does not only greatly enhance current knowledge of the thermo-elastic properties of magnetite, but it also adds the thermal EoS of a Fe^{3+}-bearing mineral to the available databases for self-consistent thermodynamic modeling (e.g., Stixrude & Lithgow-Bertelloni 2011, Holland et al. 2013) and provides a critical benchmark to ab initio approaches (e.g. Dorogokupets et al. 2016).

Recently magnetite was found to be a potentially important constituent of a phase assemblages representative of the Martian upper mantle (Xu et al. 2021). Although present only in a small amount, this experimental observation prompts for a reconsideration of the importance of magnetite for our understanding of the Martian mantle and asks for including magnetite in modeling the sound velocities and densities of a bulk assemblage representative of Mars. Noteworthy, the effects of magnetite, or of Fe^{3+}-bearing minerals more in general, were not considered in any of the *a priori* velocity models used as guidance to the interpretation of the Mars seismic records (Smrekar et al. 2019; Giardini et al. 2020; Stähler et al. 2021) due to the absence of Fe^{3+} in end-member phases in the Stixrude and Lithgow-Bertelloni (2011) database. The data collected in our study enables a more sophisticated modeling of Mars' interior at least concerning the bulk sound velocity $v_\Phi = \sqrt{K/\rho}$, where *K* corresponds to the bulk modulus and

ρ to the density, respectively. Indeed, it allows evaluating the contribution of magnetite to the seismic signal of the Martian upper mantle.

As a first example, we can consider the phase proportions proposed in Xu et al. (2021), namely 50 vol% orthopyroxene, 44 vol% olivine and 6 vol% of magnetite, representative of a Martian mantle mineralogy at a depth of ~250 km, versus a magnetite-free bulk rock containing 53 vol% orthopyroxene and 47 vol% olivine. The orthopyroxene was modeled to consist of 80 % enstatite ($MgSiO_3$) and 20 % ferrosilite ($FeSiO_3$) end-members and the olivine of 77.5 % forsterite (Mg_2SiO_4) and 22.5 % fayalite (Fe_2SiO_4) end-members, respectively (Xu et al. 2021). The change in bulk velocity was calculated using the finite strain approach with the Debye-Mie-Grüneisen model and the elastic properties for orthopyroxene and olivine reported by Stixrude and Lithgow-Bertelloni (2005, 2011) along a representative areotherm for Mars established through 3-D thermal evolution models (case 12 by Plesa et al. (2018)). This specific areotherm assumes a relatively thin average crustal thickness for Mars of 45 km, in agreement with recent findings by Knapmeyer-Endrun et al. (2021) who argue for a crustal thickness less than 40 km below the InSight lander. Generalization to different temperature profiles is straightforward. Figure 4 shows the bulk velocity of both phase assemblages versus depth. An incorporation of 6 vol% magnetite in the phase assemblage lowers the bulk velocity by ~12 m/s corresponding to ~0.21 % compared to the magnetite-free bulk assemblage. Not surprisingly, magnetite being the minor phase in the assemblages and having v_Φ very close to v_Φ of the modelled Martian assemblage (Figure S2), the effect is quite small and is well below the current seismic detection limit of the InSight mission on Mars. Nonetheless, our study improves the methodological approach, fully contributing to the general understanding and providing a deeper insight with respect to the previously uncharacterized effect of an Fe^{3+}-rich mineral on the bulk velocities of a Martian upper mantle. When considering the large diversity of possible chemical and mineralogical compositions of rocky exoplanets (e.g. Putirka and Rarick 2019),

any modeling omitting Fe^{3+}-rich minerals could result in an oversimplification, particularly in the case of planetary environments having formed in relatively oxidizing conditions. In the case of Mars, Fe^{3+}-bearing phases such as magnetite are very important for mineralogical models since they bear a signature for the redox state of Mars' mantle involving complex thermodynamic equilibrium, even when their effects of seismic velocity are minor.

Acknowledgements

We thank the technical editor, Giovanni B. Andreozzi and one anonymous reviewer for their constructive comments and G. Diego Gatta for handling the revision process of this manuscript. We thank the Sorbonne University Mineral Collection for the provision of the samples. The authors wish to thank Imène Estève for her help with sample analysis by SEM at the Institut de Minéralogie de Physique des Matériaux et de Cosmochimie (IMPMC, Paris) and Nicolas Rividi for his help during microprobe analysis at the Centre Camparis, Sorbonne Université (Paris, France). Tainá Maciel, Ludovic Delbes, Benoît Baptiste and Eglantine Boulard are acknowledged for preliminary measurements at the IMPMC X-ray diffraction platform. This project has received funding from the European Research Council (ERC) under the European Union's Horizon 2020 research and innovation Programme (Grant agreement 724690). This work was supported by the French Space Agency (CNES), focused on SEIS instrument of the InSight mission. The Scanning Electron Microscope (SEM) facility at IMPMC is supported by Région Ile de France grant SESAME 2006 N°I-07-593/R, INSU-CNRS, Institute de Physique (INP)–CNRS, University Pierre et Marie Curie–Paris 6, and by the French National Research Agency (ANR) grant ANR-07-BLAN-0124-01. This research was carried out at the P02.2 Extreme Conditions Beamline at DESY, a member of the Helmholtz Association (HGF). The research leading to this result has been supported by the project CALIPSOplus under the Grant

Agreement 730872 from the EU Framework Programme for Research and Innovation HORIZON 2020. This paper is InSight contribution 261.

References

Angel, R.J., Bujak, M., Zhao, J., Gatta, G.D., and Jacobsen, S.D. (2007) Effective hydrostatic limits of pressure media for high-pressure crystallographic studies. Journal of Applied Crystallography, 40, 26–32.

Angel, R.J., Gonzalez-platas, J., and Alvaro, M. (2014) EosFit7c and a Fortran module (library) for equation of state calculations, 229, 405–419.

Angel, R.J., Alvaro, M., Schmid-Beurmann, P., and Kroll, H. (2020) Commentary on "Constraints on the Equations of State of stiff anisotropic minerals: rutile, and the implications for rutile elastic barometry" [Miner. Mag . 83 (2019) pp. 339–347] . Mineralogical Magazine, 84, 355–357.

Boehler, R., and De Hantsetters, K. (2004) New anvil designs in diamond-cells. High Pressure Research, 24, 391-396.

Bruschini, E., Speziale, S., Andreozzi, G.B., Bosi, F., and Hålenius, U. (2015) The elasticity of $MgAl_2O_4$-$MnAl_2O_4$ spinels by Brillouin scattering and an empirical approach for bulk modulus prediction. American Mineralogist, 100, 644-651.

Dewaele, A., Loubeyre, P., and Mezouar, M. (2004) Equations of state of six metals above 94 GPa. Physical Review B - Condensed Matter and Materials Physics, 70, 1–8.

Ding, Y., Haskel, D., Ovchinnikov, S.G., Tseng, Y.C., Orlov, Y.S., Lang, J.C., and Mao, H.K. (2008) Novel pressure-induced magnetic transition in magnetite (Fe_3O_4). Physical Review Letters, 100, 18–21.

Dorogokupets, P.I., and Dewaele, A. (2007) Equations of state of MgO, Au, Pt, NaCl-B1, and NaCl-B2: Internally consistent high-temperature pressure scales. High Pressure Research, 27, 431–446.

Dorogokupets, P.I., Sokolova, T.S., Dymshits, A.M., and Litasov, K. D. (2016) Thermodynamic properties of rock-forming oxides, α-Al_2O_3, Cr_2O_3, α-Fe_2O_3, and Fe_3O_4 at high temperatures and pressures. Geodynamics and Tectonophysics, 7, 459-476.

Fei, Y., Frost, D.J., Mao, H., Prewitt, C.T., and Hausermann, D. (1999) In situ strucutre determination of the high-pressure phase of Fe3O4. American Mineralogist, 84, 203–206.

Finger, L.W., Hazen, R.M., and Hofmeister, A.M. (1986) High-Pressure crystal chemistry of spinel (MgAl2O4) and magnetite (Fe3O4): Comparisons with silicate spinels. Physics and Chemistry of Minerals, 13, 215–220.

Gatta, G.D., Kantor, I., Boffa Ballaran, T., Dubrovinsky, L., and McCammon, C. (2007) Effect of non-hydrostatic conditions on the elastic behaviour of magnetite: An in situ single-crystal X-ray diffraction study. Physics and Chemistry of Minerals, 34, 627–635.

Giardini, D., Lognonné, P., Banerdt, W. B., Pike, W. T., Christensen, U., Ceylan, S., Clinton, M., van Driel, S., Stähler, S., Böse, M., and others (2020). The seismicity of Mars. Nature Geoscience, 13(3), 205–212.

Glazyrin, K., McCammon, C., Dubrovinsky, L., Merlini, M., Schollenbruch, K., Woodland, A., and Hanfland, M. (2012) Effect of high pressure on the crystal structure and electronic properties of magnetite below 25 GPa. American Mineralogist, 97, 128–133.

Glazyrin, K., Miyajima, N., Smith, J.S., and Lee, K.K.M. (2016) Compression of a multiphase mantle assemblage: Effects of undesirable stress and stress annealing on the iron spin state crossover in ferropericlase. Journal of Geophysical Research: Solid Earth, 121, 3377-3392.

Gonzalez-Platas, J., Alvaro, M., Nestola, F., and Angel, R. (2016) EosFit7-GUI: A new graphical user interface for equation of state calculations, analyses and teaching. Journal

of Applied Crystallography, 49, 1377–1382.

Haavik, C., Stølen, S., Fjellvåg, H., Hanfland, M., and Häusermann, D. (2000) Equation of state of magnetite and its high-pressure modification: Thermodynamics of the Fe-O system at high pressure. American Mineralogist, 85, 514–523.

Holland, T. J.B., Hudson, N. F. C., Powell, R., and Harte, B. (2013) New thermodynamic models and calculated phase equilibria in NCFMAS for basic and ultrabasic compositions through the transition zone into the uppermost lower mantle. Journal of Petrology, 54(9), 1901–1920.

Huang, E., and Bassett, W.A. (1986) Rapid Determination of Fe3O4 Phase Diagram by Synchrotron Radiation. Journal of Geophysical Research, 91, 4697–4703.

Hübschle, C.B., Sheldrick, G.M., and Dittrich, B. (2011) ShelXle: A Qt graphical user interface for SHELXL. Journal of Applied Crystallography, 44, 1281–1284.

Khandarkhaeva, S., Fedotenko, T., Chariton, S., Bykova, E., Ovsyannikov, S.V., Glazyrin, K., Liermann, H.-P., Prakapenka, V., Dubrovinskaia, N., and Dubrovinsky, L. (2022) Structural Diversity of Magnetite and Products of its Decomposition at Extreme Conditions. Inorganic Chemistry, 61, 1091-1101.

Klotz, S., Chervin, J.C., Munsch, P., and Le Marchand, G. (2009) Hydrostatic limits of 11 pressure transmitting media. Journal of Physics D: Applied Physics, 42.

Knapmeyer-Endrun, B., Panning, M.P., Bissig, F., Joshi, R., Khan, A., Kim, D., Lekić, V., Tauzin, B., Tharimena, S., Plasman, M., and others (2021) Thickness and structure of the martian crust from InSight seismic data. Science, 373, 438–443.

Kouvel, J.S. (1956) Specific Heat of a Magnetite Crystal at Liquid Helium Temperatures, 106, 1489–1490.

Kuriki, A., Moritomo, Y., Ohishi, Y., Kato, K., Nishibori, E., Takata, M., Sakata, M., Hamada, N., Todo, S., Mori, N., and others (2002) High-Pressure Structural Analysis of Fe3O4. Journal of the Physical Society of Japan, 71, 3092–3093.

Larson, A.C., and Von Dreele, R.B. (2004) General structure analysis system (GSAS). Los Alamos National Laboratory Report, Report, 86–748.

Lazor, P., Shebanova, O.N., and Annersten, H. (2004) High-pressure study of stability of magnetite by thermodynamic analysis and synchrotron X-ray diffraction. Journal of Geophysical Research: Solid Earth, 109, 1–16.

Liermann, H.P., Konôpková, Z., Morgenroth, W., Glazyrin, K., Bednarčik, J., McBride, E.E., Petitgirard, S., Delitz, J.T., Wendt, M., Bican, Y., and others (2015) The Extreme Conditions Beamline P02.2 and the Extreme Conditions Science Infrastructure at PETRA III. Journal of Synchrotron Radiation, 22, 908–924.

Mao, H.-K., Takahashi, T., Bassett, W.A., Kinsland, G.L., and Merrill, L. (1974) Isothermal compression of magnetite to 320 KB. Journal of Geophysical Research, 79, 1165–1170.

Nakagiri, N., Manghnam, M.H., Ming, L.C., and Kimura, S. (1986) Nakagiri et al.1986.pdf. Physics and Chemistry of Minerals, 13, 238–244.

Otto, J., Vassiliou, J., and Frommeyer, G. (1998) Nonhydrostatic compression of elastically anisotropic polycrystals. II. Direct compression and plastic deformation. Physical Review B - Condensed Matter and Materials Physics, 57, 3264–3272.

Pasternak, M.P., Xu, W.M., Rozenberg, G.K., Taylor, R.D., and Jeanloz, R. (2003) Pressure-induced coordination crossover in magnetite; the breakdown of the Verwey-Mott localization hypothesis. Journal of Magnetism and Magnetic Materials, 265, 107–112.

Piermarini, G.J., Block, S., and Barnett, J.D. (1973) Hydrostatic limits in liquids and solids to

100 kbar. Journal of Applied Physics, 44, 5377–5382.

Plesa, A.C., Padovan, S., Tosi, N., Breuer, D., Grott, M., Wieczorek, M.A., Spohn, T., Smrekar, S.E., and Banerdt, W.B. (2018) The Thermal State and Interior Structure of Mars. Geophysical Research Letters, 45, 12,198-12,209.

Prescher, C., and Prakapenka, V.B. (2015) DIOPTAS: a program for reduction of two-dimensional X-ray diffraction data and data exploration. High Pressure Research, 35:3, 223-230.

Putirka, K.D., and Rarick, J.C. (2019) The composition and mineralogy of rocky exoplanets: A survey of >4000 stars from the Hypatia Catalog. American Mineralogist, 104, 817-829.

Rashchenko, S. V., Kurnosov, A., Dubrovinsky, L., and Litasov, K.D. (2015) Revised calibration of the Sm:SrB4O7 pressure sensor using the Sm-doped yttrium-aluminum garnet primary pressure scale. Journal of Applied Physics, 117, 2–7.

Reichmann, H.J., and Jacobsen, S.D. (2004) High-pressure elasticity of a natural magnetite crystal. American Mineralogist, 89, 1061–1066.

Rozenberg, G.K., Amiel, Y., Xu, W.M., Pasternak, M.P., Jeanloz, R., Hanfland, M., and Taylor, R.D. (2007) Structural characterization of temperature- and pressure-induced inverse normal spinel transformation in magnetite. Physical Review B - Condensed Matter and Materials Physics, 75, 2–5.

Scheidl, K.S., Kurnosov, A., Trots, D.M., Boffa Ballaran, T., Angel, R.J., and Miletich, R. (2016) Extending the single-crystal quartz pressure gauge up to hydrostatic pressure of 19 GPa. Journal of Applied Crystallography, 49, 2129-2137.

Sheldrick, G.M. (2015) Crystal structure refinement with SHELXL. Acta Crystallographica

Section C: Structural Chemistry, 71, 3–8.

Smrekar, S. E., Lognonné, P., Spohn, T., Banerdt, W. B., Breuer, D., Christensen, U., Dehant, V., Drilleau, M., Folkner, W., Fuji, N., and others (2019). Pre-mission InSights on the Interior of Mars. Space Science Reviews, 215, 1–72.

Stähler, S.C., Khan, A., Banerdt, W.B., Lognonné, P., Giardini, D., Ceylan, S., Drilleau, M.. Duran, A.C., Garcia, R.F., Huang, Q., and others (2021) Seismic detection of the martian core. Science, 373, 443-448.

Stixrude, L., and Lithgow-Bertelloni, C. (2005) Thermodynamics of mantle minerals - I. Physical properties. Geophysical Journal International, 162, 610–632.

Stixrude, L., and Lithgow-Bertelloni, C.(2011) Thermodynamics of mantle minerals - II. Phase equilibria. Geophysical Journal International, 184, 1180–1213.

Tao, R., Fei, Y., Bullock, E.S., Xu, C., and Zhang, L. (2018) Experimental investigation of Fe3+-rich majoritic garnet and its effect on majorite geobarometer. Geochimica et Cosmochimica Acta, 225, 1–16.

Toby, B.H. (2001) EXPGUI, a graphical user interface for GSAS. Journal of Applied Crystallography, 34, 210–213.

Verwey, E.J.W. (1939) Electronic Conduction of Magnetite (Fe3O4) and its Transition Point at Low Temperatures. Nature, 144, 327–328.

Xu, F., Siersch, N.C., Gréaux, S., Rivoldini, A., Kuwahara, H., Kondo, N., Wehr, N., Menguy, N., Kono, Y., Higo, Y., and others (2021) Low Velocity Zones in the Martian Upper Mantle Highlighted by Sound Velocity Measurements. Geophysical Research Letters, 48, 1–8.

Tables

Table 1: Major element composition of the natural magnetite investigated in this study reported in oxides (wt%) and atoms per formula unit (apfu) normalized to 4 oxygens.

oxides	wt%	cations	apfu
Na_2O	0.01(2)	Na	0.001(1)
CaO	0.01(3)	Ca	0.001(1)
MgO	0.05(2)	Mg	0.003(1)
MnO	0.05(4)	Mn	0.002(1)
FeO*	30.66(27)	Fe	2.985(6)
Fe_2O_3*	68.15(59)		
Al_2O_3	0.10(3)	Al	0.005(1)
Cr_2O_3	0.07(2)	Cr	0.002(1)
TiO_2	0.07(4)	Ti	0.002(1)
SiO_2	0.01(3)	Si	0.001(1)
Total	99.18(81)		4.004(6)

*initially measured as FeO and converted to FeO and Fe_2O_3 by assuming $Fe^{3+}/Fe_{tot} = 0.67$

Table 2: Unit-cell volumes of magnetite measured at listed pressures and temperatures. For the high-temperature datasets, the average of the two thermocouple readings was assumed as the sample's temperature and the standard deviation were taken as uncertainties. The pressure uncertainties were determined by the half difference between the measurements of the pressure standards taken before and after each XRD measurement.

P (GPa)	*T* (K)	*V* Å^3
	DAC_300Kpwd	
0.0001(1)	298	592.45(17)
0.41(1)	298	591.22(23)
0.99(1)	298	589.56(25)
1.82(1)	298	585.78(21)
2.76(1)	298	583.99(25)
3.45(1)	298	581.87(12)
4.28(3)	298	579.37(16)
5.10(1)	298	577.32(19)
6.06(1)	298	574.52(16)
7.42(11)	298	570.46(14)
7.87(1)	298	568.97(21)
8.89(1)	298	566.30(25)
10.02(3)	298	562.98(22)
11.04(1)	298	560.55(28)
11.66(61)	298	558.63(39)
12.78(1)	298	557.11(19)
13.12(1)	298	556.12(23)
14.14(1)	298	553.86(14)
14.87(6)	298	552.57(14)
	DAC_300Ksc	
0.0001(1)	298	592.26(6)

0.77(1)	298	590.04(6)
1.65(1)	298	587.07(8)
3.00(3)	298	583.82(8)
3.97(8)	298	579.41(8)
5.69(6)	298	574.58(8)
6.69(14)	298	572.20(6)
7.66(9)	298	570.05(8)
8.71(9)	298	567.60(8)
9.89(1)	298	563.42(8)
10.99(6)	298	561.01(6)
12.02(6)	298	559.68(6)
13.21(1)	298	555.82(6)
14.40(1)	298	553.65(8)
15.74(3)	298	550.27(5)
	DAC_600K	
1.11(1)	298	589.77(8)
1.77(1)	601(50)	591.86(8)
2.47(1)	601(50)	589.45(8)
3.73(1)	603(50)	585.58(8)
4.09(1)	604(50)	583.50(8)
5.62(8)	604(50)	580.39(8)
6.90(16)	602(50)	576.45(10)
7.54(1)	601(50)	575.08(10)
8.85(8)	600(50)	570.82(10)
9.38(4)	600(50)	569.97(14)
11.43(8)	598(50)	564.50(16)
12.49(12)	597(50)	561.52(18)
12.99(4)	598(50)	560.98(10)
	DAC_900K	
3.61(1)	883(59)	593.23(22)

5.06(1)	858(57)	586.92(16)
6.00(1)	873(57)	586.30(11)
7.04(1)	872(57)	583.43(8)
7.98(1)	866(57)	580.26(8)
9.02(1)	867(57)	578.04(47)
9.74(1)	866(56)	575.94(11)
10.97(1)	869(57)	570.63(24)
12.33(1)	869(56)	568.09(19)
13.50(1)	867(56)	564.89(18)
	DAC_1100K	
1.75(1)	574(50)	591.67(4)
2.29(1)	687(50)	592.33(4)
2.84(1)	772(57)	592.60(5)
3.40(1)	874(68)	593.16(5)
3.91(1)	977(63)	593.91(6)
4.33(1)	1075(65)	594.60(6)
4.82(1)	1072(66)	592.85(5)
5.59(1)	1060(67)	590.51(4)
6.27(1)	1069(70)	589.96(6)
6.64(1)	1064(70)	586.96(5)
7.34(1)	1078(72)	586.10(6)
7.93(1)	1071(72)	583.10(6)
8.27(1)	1068(72)	583.16(7)
8.82(1)	1062(72)	580.43(7)
9.58(1)	1072(74)	579.41(9)
10.39(1)	1065(75)	575.86(13)

Figures

Figure 1a

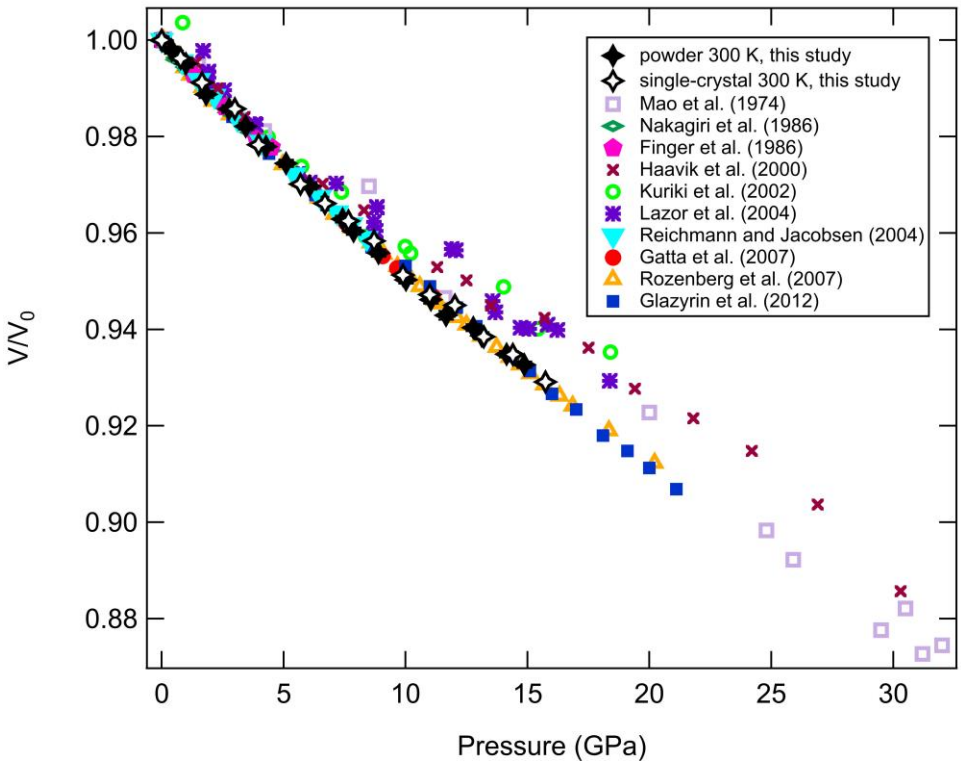

Figure 1b

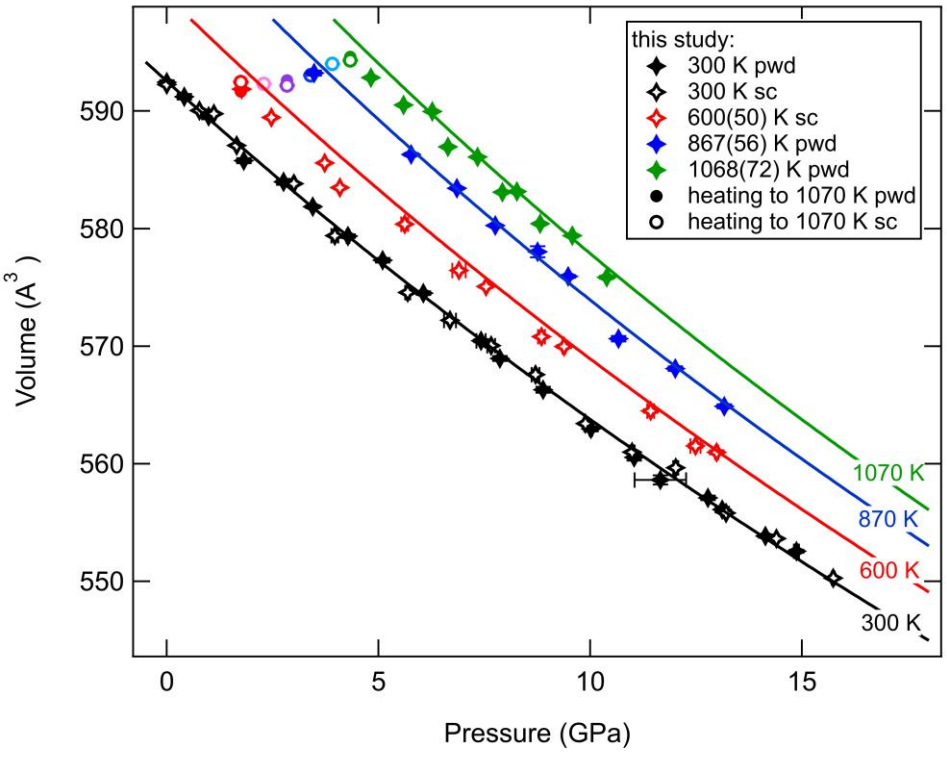

Figure 1: a) Pressure evolution of the unit-cell volume of magnetite at 300 K. Values obtained in this study, normalized with respect to the room pressure measurement, (black open and closed symbols) are compared to literature data (colored symbols). Data obtained from powder X-ray diffraction (Mao et al. 1974; Nakagiri et al. 1986; Haavik et al. 2000; Kuriki et al. 2002; Lazor et al. 2004; Rozenberg et al. 2007; this study) are shown as open symbols and single-crystal data (Finger et al. 1986; Reichmann and Jacobsen 2004; Gatta et al. 2007; Glazyrin et al. 2012; this study) are plotted as closed symbols. b) High-pressure and high-temperature volume of Fe_3O_4 magnetite obtained in this study. High-temperature data collected upon heating to 1100 K are shown as color-coded circles for increasing temperature: red = 574(50) K, rose = 687(50) K, purple = 772(57) K, blue = 874(68) K, light blue = 977(63) K, green = 1075(65) K. Lines across experimental points are the outcome of fitting to a BM2 EoS combined with a Mie-Grüneisen-Debye (MGD) model for the thermal pressure (see text for details).

Figure 2a

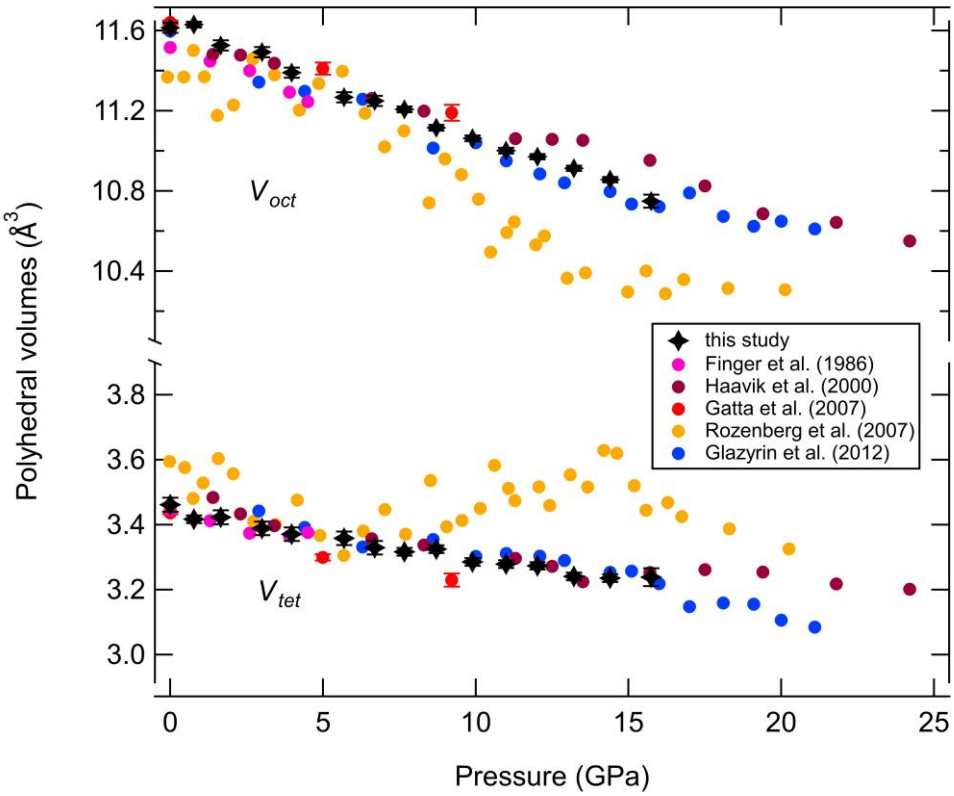

Figure 2b

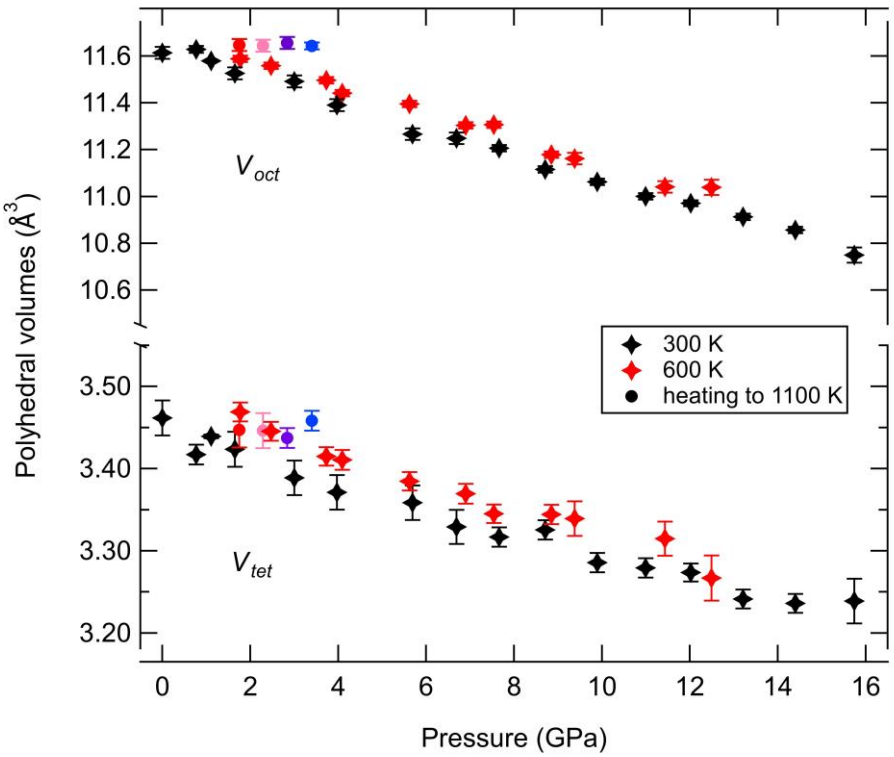

Figure 2: a) Pressure evolution of the volume of the octahedral (V_{oct}) and tetrahedral (V_{tet}) sites measured in this study (black symbols) and literature data (colored symbols, Finger et al. 1986; Haavik et al. 2000; Gatta et al. 2007; Rozenberg et al. 2007; Glazyrin et al. 2012). b) Polyhedral volumes measured in this study at high pressure and high temperature. Data collected upon heating follows the same color code as reported in Figure 1b.

Figure 3

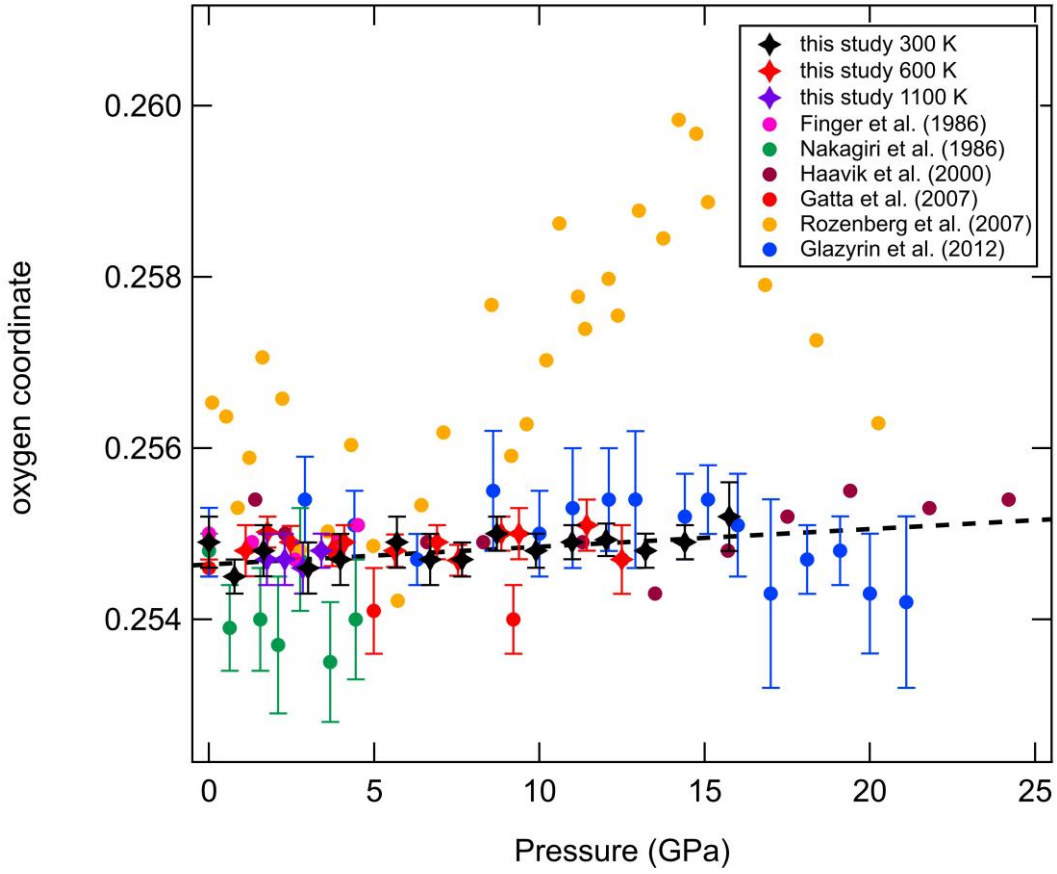

Figure 3: Comparison of the evolution of the oxygen fractional coordinate *u* with increasing pressure obtained using data collected in this study (both room temperature and high-temperature) and reported in the literature (Finger et al. 1986; Nakagiri et al. 1986; Haavik et al. 2000; Gatta et al. 2007; Rozenberg et al. 2007; Glazyrin et al. 2012). The dashed line is a

guide to the eye showing the evolution of *u* with pressure at ambient temperature observed in this study.

Figure 4

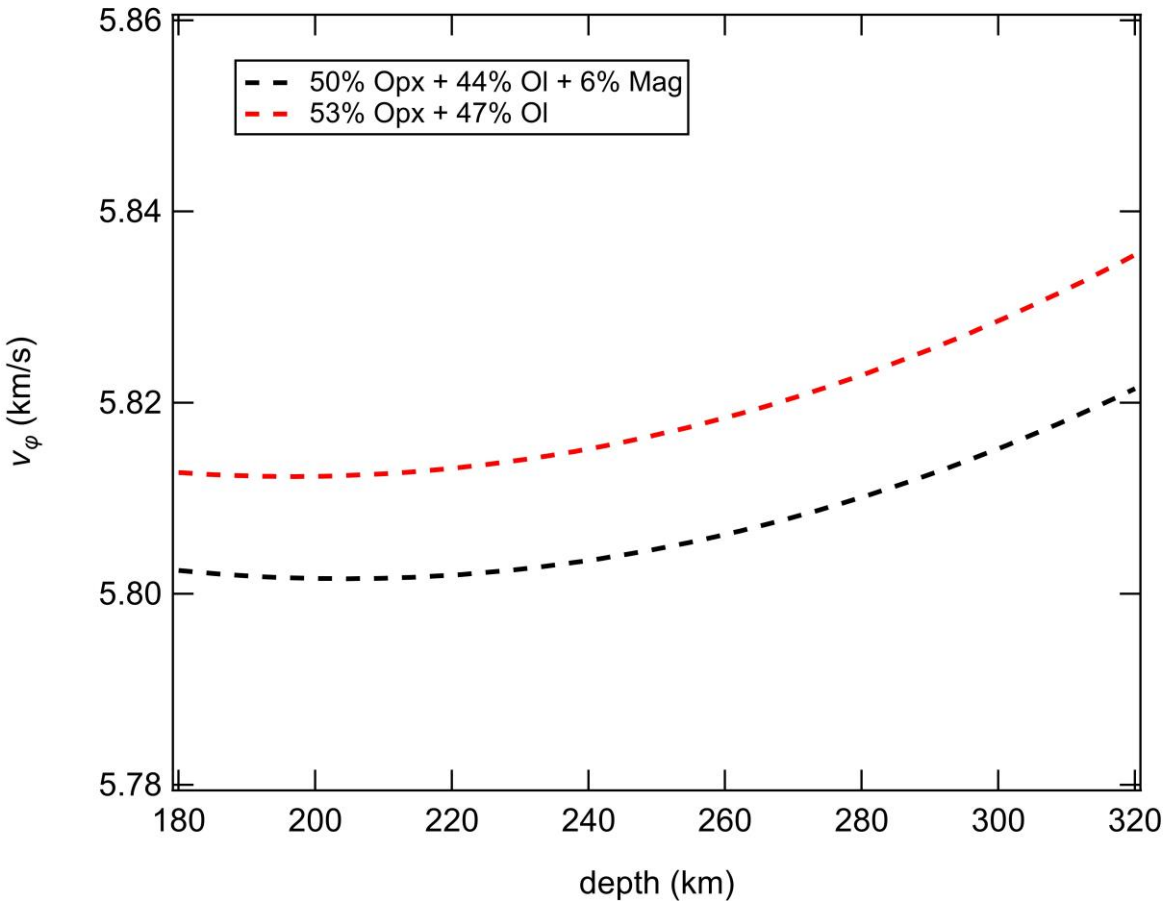

Figure 4: Bulk velocity v_Φ versus depth calculated along areotherm case 12 proposed for Mars (Plesa et al. 2018) for two phase assemblages: i) 50 % orthopyroxene, 44 % olivine and 6 % magnetite (black) and ii) magnetite-free bulk assemblage made by 53 % orthopyroxene and 47 % olivine (red).

Supplementary Information

Figure S1

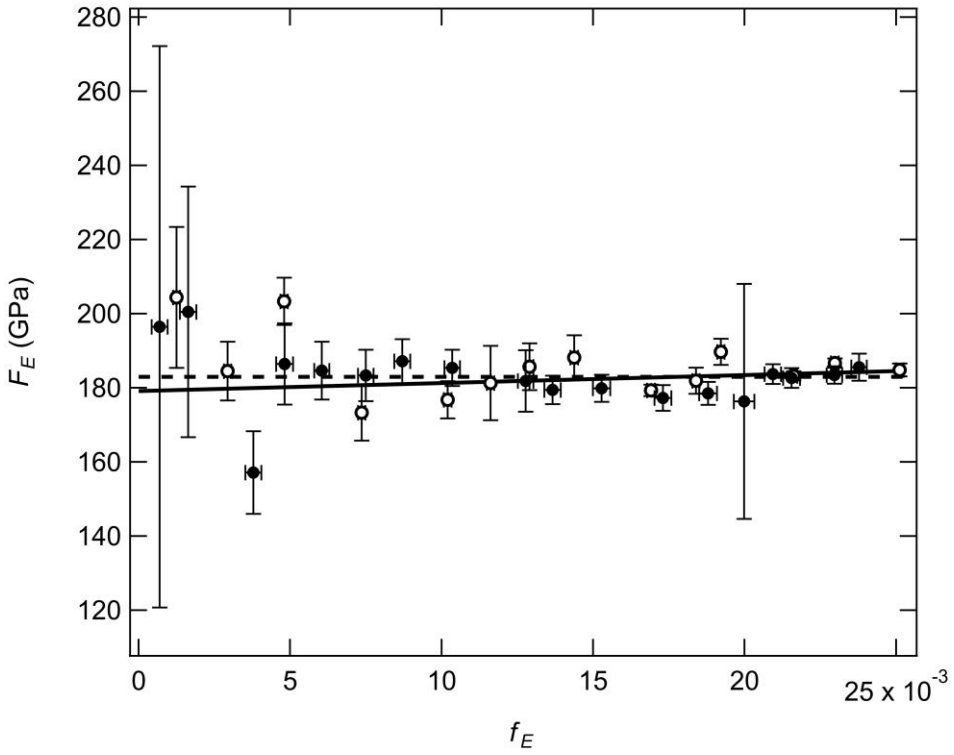

Figure S1: Normalized pressure (F_E) plotted against the Eulerian strain (f_E) for Fe_3O_4 magnetite measured at ambient temperature. The solid circles indicate data collected on a powdered magnetite sample whereas the open circles indicate data obtained from a single-crystal of magnetite. The lines represent 2nd (dashed) and 3rd (solid) order Birch-Murnaghan fits through the dataset.

Figure S2

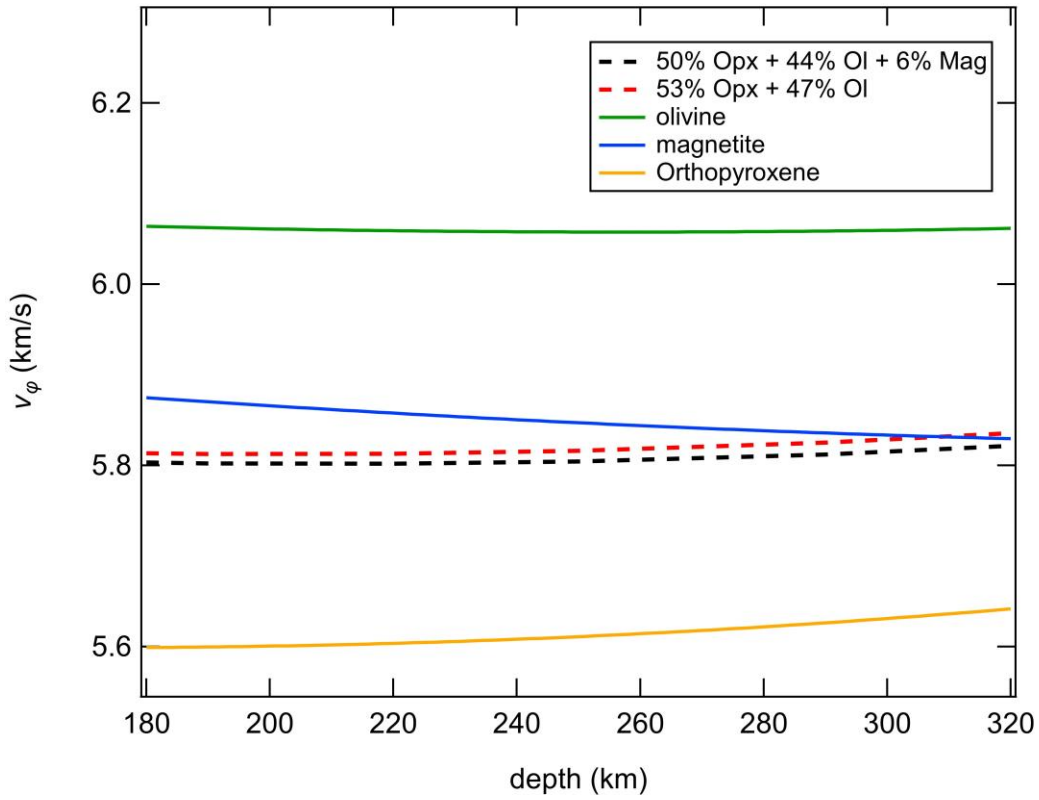

Figure S2: Bulk sound velocity v_Φ calculated versus depth along areotherm case 12 proposed for Mars (Plesa et al. 2018) for olivine (Fo77.5, green), magnetite (blue) and orthopyroxene (En80, orange). These bulk velocities are compared to the two phase assemblages 1) containing 50 % orthopyroxene, 44 % olivine and 6 % magnetite (black) and 2) a magnetite-free bulk assemblage with 53 % orthopyroxene and 47 % olivine (red) as shown in Figure 4.

Table S1: Single-crystal unit-cell volumes of magnetite measured at different pressures and temperatures, oxygen coordinate *u*, R_{int} and *R1* and the number of unique reflections obtained in the structural refinements.

P (GPa)	*T* (K)	*V* (Å^3)	*u* (-)	R_{int} (%)	*R1 (%)*	*No. Unique reflections*
			DAC_300Ksc			
0.0001(1)	298	592.26(6)	0.2549(3)	3.59	2.44	28
0.77(1)	298	590.04(6)	0.2545(2)	3.14	2.28	29
1.65(1)	298	587.07(8)	0.2548(3)	3.61	2.63	30
3.00(3)	298	583.82(8)	0.2546(3)	2.59	2.70	30
3.97(8)	298	579.41(8)	0.2547(3)	2.76	2.70	30
5.69(6)	298	574.58(8)	0.2549(3)	3.19	2.43	28
6.69(14)	298	572.20(6)	0.2547(3)	4.20	2.29	27
7.66(9)	298	570.05(8)	0.2547(2)	2.38	2.41	27
8.71(9)	298	567.60(8)	0.2550(2)	2.71	1.93	26
9.89(1)	298	563.42(8)	0.2548(2)	3.34	2.38	27
10.99(6)	298	561.01(6)	0.2549(2)	4.66	2.62	27
12.02(6)	298	559.68(6)	0.25493(2)	2.67	1.79	27
13.21(1)	298	555.82(6)	0.2548(2)	2.43	2.70	29
14.40(1)	298	553.65(8)	0.2549(2)	2.58	2.27	27
15.74(3)	298	550.27(5)	0.2552(4)	3.18	2.49	28
			DAC_600K			
1.11(1)	298	589.77(8)	0.2548(3)	1.82	1.80	38

1.77(1)	601(50)	591.86(8)	0.2550(2)	2.40	1.83	37
2.47(1)	601(50)	589.45(8)	0.2549(2)	2.99	1.77	37
3.73(1)	603(50)	585.58(8)	0.2548(2)	2.07	1.62	38
4.09(1)	604(50)	583.50(8)	0.2549(2)	2.41	1.56	37
5.62(8)	604(50)	580.39(8)	0.2548(2)	1.60	1.44	37
6.90(16)	602(50)	576.45(10)	0.2549(2)	1.98	1.94	36
7.54(1)	601(50)	575.08(10)	0.2547(2)	2.14	2.16	39
8.85(8)	600(50)	570.82(10)	0.2550(2)	3.07	2.46	34
9.38(4)	600(50)	569.97(14)	0.2550(3)	2.79	2.60	34
11.43(8)	598(50)	564.50(16)	0.2551(3)	2.76	2.22	35
12.49(12)	597(50)	561.52(18)	0.2547(4)	4.54	2.77	33
			DAC_1100K			
1.75(1)	574(50)	592.47(6)	0.2547(3)	4.13	3.85	29
2.29(1)	687(50)	592.32(6)	0.2547(3)	3.80	3.59	33
2.84(1)	772(57)	592.17(6)	0.2546(3)	2.52	3.56	36
3.40(1)	874(68)	593.04(6)	0.2548(2)	3.81	1.89	30